

Ultra-low threshold continuous-wave quantum dot mini-BIC lasers

Hancheng Zhong¹, Jiawei Yang¹, Zhengqing Ding¹, Lidan Zhou¹, Yingxin Chen¹, Ying Yu^{1*},
Siyuan Yu^{1*}

¹ State Key Laboratory of Optoelectronic Materials and Technologies, School of Electronics and Information Technology, Sun Yat-Sen University, Guangzhou 510275, China

Highly compact lasers with ultra-low threshold and single-mode continuous wave (CW) operation have been a long sought-after component for photonic integrated circuits (PICs). Photonic bound states in the continuum (BICs), due to their excellent ability of trapping light and enhancing light-matter interaction, have been investigated in lasing configurations combining various BIC cavities and optical gain materials. However, the realization of BIC laser with a highly compact size and an ultra-low CW threshold has remained elusive. We demonstrate room temperature CW BIC lasers in the 1310 nm O-band wavelength range, by fabricating a miniaturized BIC cavity in an InAs/GaAs epitaxial quantum dot (QD) gain membrane. By enabling effective trapping of both light and carriers in all three dimensions, ultra-low threshold of 12 μW (0.052 kW/cm^2) is achieved. Single-mode lasing is also realized in cavities as small as only 5×5 unit-cells ($\sim 2.5\times 2.5 \mu\text{m}^2$ cavity size) with a mode volume of $1.16(\lambda/n)^3$. With its advantages in terms of a small footprint, ultralow power consumption, robustness of fabrication and adaptability for integration, the mini-BIC lasers offer a perspective light source for future PICs aimed at high-capacity optical communications, sensing and quantum information.

Lasers with ultra-low threshold and compact size are highly desirable in photonic integrated circuits (PICs)¹⁻³, aiming at the application of optical communications^{4, 5}, chip-scale solid-state LIDAR⁶, and quantum information^{7, 8}. The general approach to realizing such lasers is to effectively trap light and boost light-matter interaction by embedding gain materials into few- or sub-wavelength scale optical cavities with high quality (Q) factor and/or small mode volume (V-mode)^{2, 9, 10}. Among different types of cavities, a photonic crystal (PhC) slab consisting of periodic dielectric structures is a versatile platform to achieve high Q factor via introducing defect-type PhC modes¹¹⁻¹⁴ or photonic bound states in the continuum (BICs) modes¹⁵⁻²¹. The former achieves lateral confinements using distributed Bragg reflection and out-of-plane confinement based on total internal reflection and the latter are formed based on topological mechanisms of either symmetry protection or destructive interference (accidental BIC mode). For lasing action, the reported defect-type PhC lasers, while exhibiting extremely small V-mode and therefore ultra-low threshold^{12, 22, 23}, nevertheless suffers instability caused by sensitivity to the structural disorder²⁴. In this regard, BIC lasers that may benefit from topological robustness¹⁸ are one of the most promising alternative architectures. However, radiative BIC (quasi-BIC) modes in PhC slabs²⁵⁻³¹ or gratings³²

with high Q-factor are often realized requiring symmetry in the vertical (thickness) direction and extended lateral periodic structures to reduce in-plane light leakage, therefore intrinsically limiting their footprint to hundreds of unit-cells.

A further factor impeding the performance of BIC lasers is the poor carrier confinement and pumping efficiency. In contrast to defect cavity PhC lasers where the light is localized therefore effective carrier confinement can be achieved by burying the gain medium in the defect cavity only^{33, 34}, BIC lasers, with its modes diffusely distributed across the cavity, require optical gain (therefore carriers) distributed across the structure. The high surface-volume ratio results in high non-radiative recombination of carriers. Therefore, reported conventional BIC lasers displayed relatively low pumping efficiency, high lasing thresholds and were limited to operating under femto- or pico-second pulse pumping²⁵⁻³², imposing a great challenge in advancing photonic integration applications that requires highly compact and low threshold lasers.

Such challenges have recently been alleviated to some extent by merging the two BIC modes (super-BICs)³⁵ or combining the BIC mode with other mirror-like reflection either by Fano-mirror³⁶, or by photonic heterostructure³⁷. The super-BIC laser³⁵ demonstrated relatively low threshold, but still pulse-pumped, lasing in InGaAsP PhC slab with a footprint of (40×40) unit cells. The Fano BIC laser³⁶ demonstrated excellent coherent profile and a threshold of ~12 kW/cm² under continuous-wave (CW) pumping but required localizing the gain in the continuum region by utilizing semiconductor buried heterostructure to protect the spatial asymmetry of the Fano BIC mode. The BIC laser in photonic heterostructure³⁷ has scaled down the diameter of fundamental mode to ~30 unit-cells, however the challenge is from the instability of the monolayer transition metal dichalcogenide gain material. A scalable, CW operated, highly compact, and ultra-low threshold BIC laser has therefore remained elusive.

Very recently, a new kind of BIC mode termed as miniaturized BICs (mini-BICs)³⁸ was proposed, which combines a traditional BIC mode and a lateral photonic bandgap mirror in a cooperative way to trap light in all three dimensions, achieving a record high Q factor and rather small V-mode in silicon-based passive structures³⁸. On the other hand, epitaxial quantum dot (QD) materials, due to their ability to three-dimensional confinement of carriers, have lower threshold³⁹, high temperature stability^{40, 41}, and in particular high tolerance to epitaxial defects or etching-induced surface defects⁴²⁻⁴⁴, therefore could serve as an efficient gain material for BIC lasers by suppressing nonradiative recombination paths.

In this work, we present the realization of CW operated BIC lasers with low-thresholds and small V-modes by combining O-band InAs/GaAs epitaxial QD gain material with mini-BIC cavities. Benefitting from the three-dimensional confinement of both light and carriers provided by the mini-BIC cavity and the QD, we achieve CW single mode operation by tuning the lattice constant and the cavity size to match the cavity mode frequency to the heterostructure bandgap. CW lasing threshold as low as 12 μ W (0.052 kW/cm²) is achieved when the resonant wavelength just at the peak of QD material gain spectrum. Single-mode mini-BIC lasers with the cavity size down to 5×5 unit-cells (~2.5×2.5 μ m²) are also demonstrated, exhibiting a mode volume as low as 1.16(λ/n)³. These mini-BIC QD lasers with their small footprint, low power

consumption and robustness in fabrication could contribute to the development of high density integrated light sources on photonic integrated circuit (PIC) chips.

Device operational principle

A schematic of our mini-BIC laser is shown in **Fig. 1a**. The mini-BIC cavity is fabricated in a three-layer InAs/GaAs QD stack with a density of $5.5 \times 10^{10}/\text{cm}^2$ per layer (the right panel of **Fig. 1a**) and a thickness h of 556 nm. The PhC slab is embedded in the middle of an ultraviolet curing adhesive (Norland Optical Adhesive, NOA) with a refractive index of 1.54, to provide mirror-flip symmetry in the vertical direction. The in-plane cavity is formed by a PhC heterostructure, which consists of a square-lattice array of nanoholes (region A) surrounded by a boundary region (region B) with a transition region between them. **Fig. 1b** plots the calculated band diagrams of infinite PhC slabs that have the same lattice constants as regions A and B. Here the diameter of hole r is 390 nm, and the lattice constant of regions A and B are set as $a=495$ nm and $b=530$ nm respectively. We choose the lowest-frequency fundamental TE mode in region A (TE A) as the lasing mode due to its larger feedback strength (coupling constant) and thus lower threshold than other higher-order modes^{45, 46}. The frequency of TE A is tuned so that it falls within the gain spectral range of the O-band InAs/GaAs QDs with its peak in the vicinity of 1300 nm (See Supplementary Information Fig. S1).

To achieve effective light-trapping in the transverse direction, the energy of TE A, which is above the light cone of region A (shaded green region in **Fig. 1b**), is designed to be inside the bandgap of region B (TE B) that forbids lateral leakage (yellow region in **Fig. 1b**), so that region B acts as an almost perfectly reflective mirror. Different from the continuous bands in infinite PhC slabs, eigenstates of the confined PhC in region A are a series of discrete modes, as the continuous momentum space is quantized into isolated points with a spacing of $\delta k = \pi/L$, where $L = N_a \cdot a$ is the cavity length of region A. Therefore, each discrete mode can be represented by a pair of quantum numbers (p , q) or defined as M_{pq} , indicating that it is localized near $(p\pi/L, q\pi/L)$ in the first quadrant of the momentum (k) space. **Fig. 1c** shows a typical distribution of four eigenmodes (M_{11} , M_{12}/M_{21} and M_{22}) in the k -space, in which the modes of M_{12} and M_{21} are degenerate in energy due to the C_4 symmetry of the structure. Here the number of holes along the side of regions A and B is set as $N_a=13$ and $N_b=10$ respectively, and the gap between the two regions is fixed as $(a+b)/2$. The corresponding calculated mode magnetic field H_z profiles of M_{11} , M_{12}/M_{21} and M_{22} are plotted in **Fig. 1d**, indicating V-modes of $7.46(\lambda/n)^3$, $7.43(\lambda/n)^3$ and $7.40(\lambda/n)^3$, respectively.

To further reduce cavity volume as well as search for single mode operation, we explore the effect of device size and lattice constant on the modes of the mini-BIC structure. We simulate a series of structures with N_a varying from 15 to 5 and a from 495 nm to 485 nm. As shown in **Fig. 1e**, the decrease of N_a results in the increase of δk (equal to π/L), moving all modes outwards away from the center Γ point with increasing mode intervals. Only one mode, M_{11} , settles inside the bandgap of region B when N_a decreases to 7, which indicates that single mode lasing may be realized in a smaller cavity with $N_a=7$ or 5.

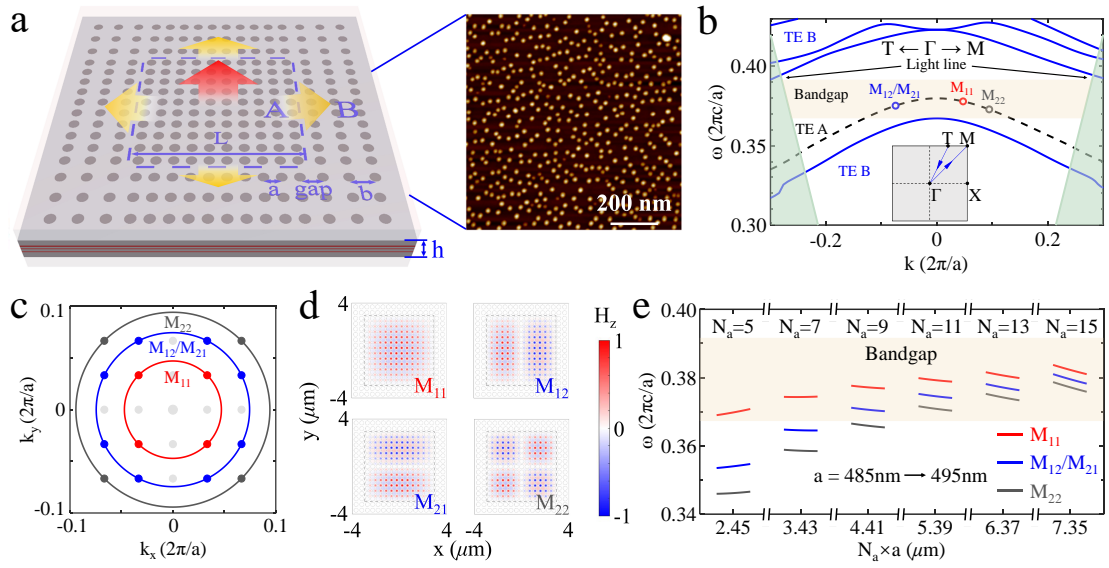


Figure 1. The theoretical scheme of mini-BIC laser structure. **a.** Schematic of a mini-BIC cavity (region A) encircled by a boundary of photonic bandgap (region B) to form a photonic heterostructure. The cavity region A is a $N_a \times N_a$ array of square latticed circular holes with the period of a and side-length of L , while the boundary region B is an array with a width of N_b and a period of b , but shares the same period of a in the connecting side with region A. The circular holes of the PhC slab, whose radii equal to r , are etched in an InAs/GaAs QD active layer with thickness $h = 556$ nm. The PhC slab is designed to be immersed in NOA. An atomic force microscopy (AFM) image of uncapped InAs/GaAs QDs (the right panel) indicates QD density of $5.5 \times 10^{10}/\text{cm}^2$. **b.** The calculated band diagrams of infinite PhC slabs: the continuous band (TE A, represented by the black dashed line) of an infinitely large PhC splits into a series of discrete modes above the light line and located in the bandgap of region B (TE B, represented by the blue solid line). **c.** The momentum distribution of each mode, labeled as M_{pq} according to their location in the first quadrant of momentum space. **d.** Calculated H_z near-field distributions of M_{11} , M_{12} , M_{21} and M_{22} at $a = 495$ nm in a finite-size cavity with $N_a = 13$. **e.** Simulated mode frequencies of mini-BIC structures with N_a varying from 15 to 5 and the lattice constant varying from 495 nm to 485 nm. The mode intervals increase with decreasing N_a and only one mode of M_{11} settles inside the bandgap when N_a decreases to 7, indicating that single mode lasing may be realized in a small cavity with $N_a = 5$ or 7.

Lasing performance characterization

In experiment, the whole structure was fabricated on a GaAs-on-Glass platform using membrane transfer technique (details in Method section and Supplementary Information Fig. S2). To generate accidental BIC mode in experiment, the PhC membrane is placed in the middle of $\sim 5 \mu\text{m}$ NOA ($n_{\text{NOA}} = 1.54$) and sandwiched between two glass plates ($n=1.49$) to ensure the mirror-flip symmetry^{17, 47}. **Fig. 2a** shows a typical top-view scanning electron microscopy (SEM) images of the fabricated mini-BIC cavity with $N_a = 13$. The photonic heterostructure of the mini-BIC laser can be clearly seen in the optical microscopy image as shown in the lower panel of **Fig. 2a**. The micro-photoluminescence (μ -PL) measurements are performed using a 705-nm CW laser with a spot size of $\sim 5.4 \mu\text{m}$ at room temperature (details in Method section and Supplementary Information Fig. S3). **Fig. 2b** demonstrates the evolution of the

emission spectrum under various pumping power of a mini-BIC laser with $a = 495$ nm and $N_a = 13$. A broad, spontaneous emission peak centered at 1303 nm is observed at low pumping intensities. With increasing pumping power, two sharp peaks appear at 1303 nm and 1316 nm (the resonant wavelengths of M_{11} and M_{12}/M_{21}) and quickly dominates the emission spectrum with an overall suppression of the photolumuminescence. At higher pump power, the weak peaks of other modes with larger quantum numbers (p and q) can also be excited, such as M_{22} at 1326 nm and M_{13}/M_{31} at 1333nm. It's worth noting that fabrication imperfections would slightly break the C4 symmetry and thus split the theoretically degenerate mode peaks of M_{12}/M_{21} (**Fig. 2b**) with a minimal energy difference.

Fig. 2c shows the evolution of the output laser intensity (light in-light out (L-L) curve) and the linewidth of M_{11} mode as a function of the pumping power, exhibiting a clear lasing behavior with a threshold power of $52 \mu\text{W}$ ($0.227 \text{ kW}/\text{cm}^2$). The linewidth decreases from ~ 2.4 nm at low pumping power to 0.48 nm just below the threshold (the inset in **Fig. 2c**), which suggests a spectral linewidth narrowing effect during lasing and a cavity Q factor of 2715. The deviation between the simulated and measured Q factors (Supplementary Information Fig. S4) may be attributed to the vertical leakage and scattering loss caused by the inevitable fabrication imperfections. Nevertheless, due to the lateral light trapping by the photonic heterostructure, this measured Q factor is much larger than that from the structure without region B (Supplementary Information Fig. S5). Furthermore, the nearly constant lasing wavelength across the range of pumping power (less than 1.6 nm/mW in **Fig. 2d**) indicates that thermal effect was almost negligible in our devices, which may be attributed to the high temperature stability of QDs as well as the improved heat dissipation of our embedded BIC cavities compared with conventional suspended QD-PhC lasers²³, as the NOA has relatively higher thermal conductivity compared to air.

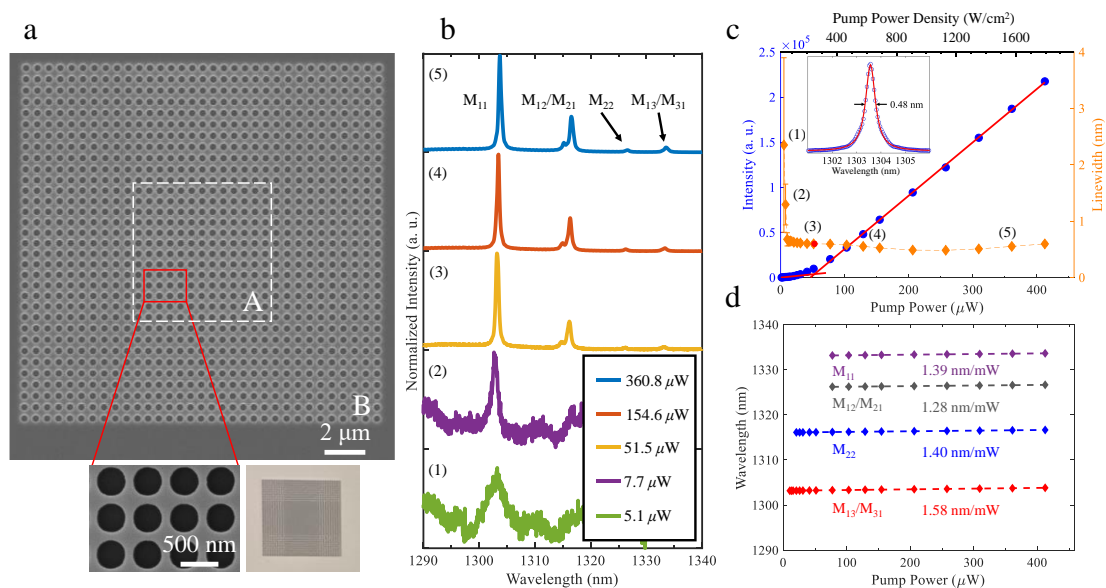


Figure 2. Fabricated sample and the mini-BIC laser performance. **a.** Scanning electron microscopy (SEM) images of the mini-BIC laser with $a = 495$ nm and $N_a = 13$, the inset illustrates a magnified view of the cavity region. The photonic heterostructure of the mini-BIC lasers can be clearly seen in the optical microscopy image (the lower

panel). **b.** Measured emission spectra under various pumping power. **c.** The collected emission intensity and the linewidth of the lasing M_{11} peak at 1303 nm as a function of pumping power, indicating a lasing threshold of 52 μW (227 W/cm^2). The inset is a Lorentzian curve fitting of the spectra just below the threshold, which indicates a linewidth of ~ 0.48 nm and therefore a cavity Q factor of 2715. **d.** The lasing wavelengths of each mode under various input pumping powers (diamonds) and their linear fit (dashed lines). The error bars in **c** and **d** correspond to standard errors deduced by fitting.

Single mode lasing with small footprint

To experimentally demonstrate single mode lasing and wavelength tunability, we vary the lattice constant a from 495 nm to 485 nm in 2-nm steps and with N_a changing from 5 to 15, resulting in a total of 36 devices that can be measured. The measured wavelengths of the all four modes agree well with the theoretical resonant wavelengths, which confirms that lasing action is indeed from the min-BIC discrete modes. As N_a decreases, the wavelength of all modes shows a red-shift away from the wavelength at the Γ point and simultaneously, the mode intervals increase due to the larger δk (See Supplementary Information Fig. S6). Accordingly, fewer modes appear within the gain spectrum and thus fewer lasing modes are exhibited in the structure with smaller N_a . **Fig. 3a** further demonstrates the typical measured lasing wavelength of M_{11} mode of mini-BIC cavities with different sizes and different lattice constants, where a wide tunable range near 80 nm is achieved, with highly predictable wavelengths. As expected, the experimental lasing wavelengths of M_{11} red shift as a increases due to the decreasing resonant frequency of TE A. The measured threshold powers of the lasers shown in **Fig. 3b** generally lie in the range of 12-75 μW except for the few far outlying in the long wavelengths and have a minimum close to the central wavelength of the ground state of the QD gain materials, where maximum gain is afforded by the strong zero-dimensional carrier confinement. Notably, an ultra-low threshold of 12 μW (0.052 kW/cm^2) is observed in the mini-BIC laser with $a = 487$ nm and $N_a = 7$, with a Q factor of 790 and a cavity mode exactly located at the peak (1300 nm) of the QD gain spectra (yellow region). A weak peak of M_{12}/M_{21} mode at 1328 nm can be observed at high pump power (**Fig. 3c**), which may be attributed to the imperfect lateral optical confinement caused by insufficient number of periods ($N_b=10$) in region B. Single mode lasing is eventually achieved with the cavity size down to 5×5 unit-cells ($\sim 2.5 \times 2.5 \mu\text{m}^2$ with a mode volume of $1.16(\lambda/n)^3$). The L-L curve and lasing spectra of the device with $a = 485$ nm are shown in **Fig. 3d**, exhibiting a threshold of 17 μW (0.074 kW/cm^2) and single-mode lasing across the range of pumping intensity up to 200 μW (12x threshold). More lasing spectra can be found in Supplementary Information Fig. S7.

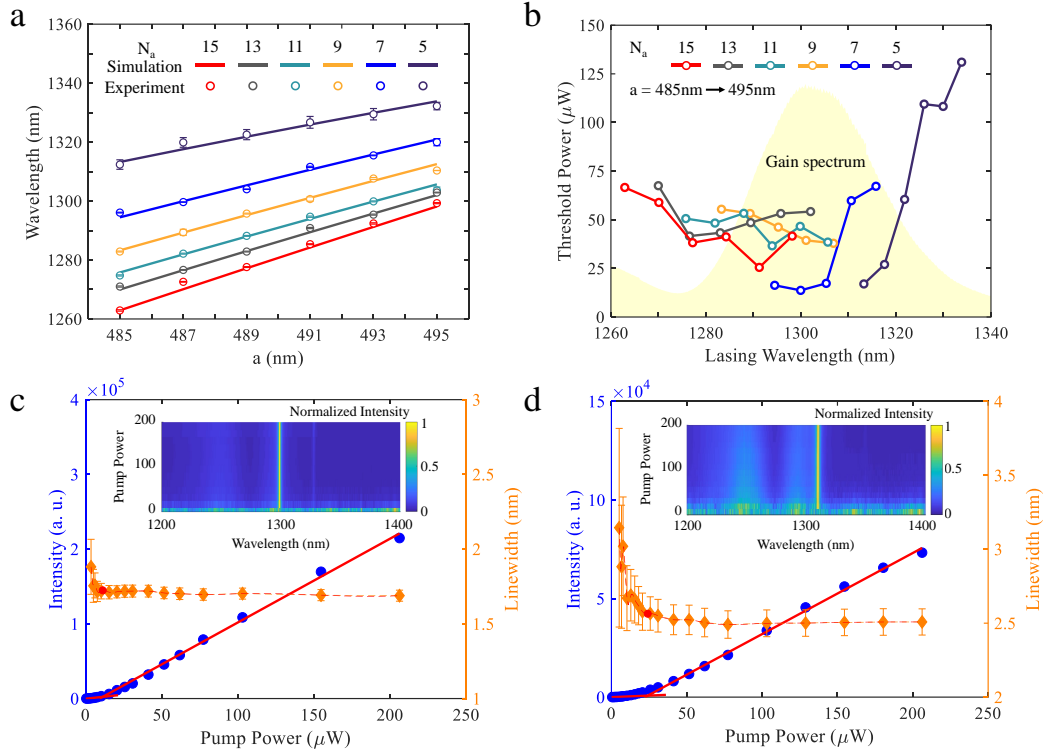


Figure 3. Wavelength tunability and single mode lasing with small footprint. **a.** The typical measured lasing wavelengths of M_{11} mode in the cavities of different sizes and different periods agree well with theoretical resonant wavelengths. A wide tuning range of nearly 80 nm is achieved, with highly predictable wavelengths. **b.** The measured threshold power of the lasers with different a and N_a . The yellow shaded region shows the relative magnitude of the QD gain spectrum. The threshold increases markedly for wavelengths longer than 1320 nm, where the optical gain of the QD ground state fall off sharply. On the short wavelength side, the threshold rises slowly as some gain results from the excited state of the QDs. **c-d.** The evolution of the collected emission intensity, linewidth as well as intensity spectrum as a function of pump power of the samples with $a = 487$ nm and $N_a = 7$ (c) and $a = 485$ nm and $N_a = 5$ (d).

Enhancement of the Q factor by topological engineering

It is worth mentioning that the ultra-low threshold or single-mode operation data presented above represent some of the worst-case results in term of cavity Q factor, which on one hand confirms the robustness of the mini-BIC laser and on the other hand indicates that the mini-BIC lasers could be further improved to achieve even lower threshold.

Fundamentally, the Q factor could be further improved by the enhanced vertical light confinement, that is, the mini-BIC modes can be designed to converge with accidental BIC modes^{18, 35, 38} by fine-tuning the lattice constant of region A. Taking the samples with a fixing N_a of 13 and different lattice constant a for example, as plotted in **Fig. 4a**, the high-Q ring arising from topological constellation shrinks towards Γ point as lattice constant a increases and eventually reaches the states of M_{11} at $a=495$ nm. Theoretically, extremely high Q factor of $\sim 10^{10}$ can be achieved in an ‘empty’ (i.e., no material loss) cavity due to this full three-dimensional light confinement. The theoretical trajectory of M_{11} mode as a function of N_a is labeled as circles along the Γ -M direction in the upper

panel of **Fig. 4b**, where the momentum of M_{11} with $N_a = 13$ should be nearest to the accidental BIC mode at $k = 0.057$. However, the measured Q factor, as shown in the lower panel of **Fig. 4b**, only shows an increase with the cavity size as the mode moves close to Γ point, without demonstrating the effect of the merge between the M_{11} mode with the accidental BIC. We also track how the Q factor of M_{11} changes with increasing lattice constant a at varied N_a , and find it almost monotonically increases from $a = 485$ nm to $a = 495$ nm (**Fig. 4c**).

As mentioned, the experimental Q values in the range of 500-3000, which is far lower than above theoretical values of $Q_{\text{intrinsic}}$, are attributable to additional extrinsic losses caused by the vertical leakage and scattering losses due to the inevitable fabrication imperfections. For high Q cavities, the losses are additive and the Q factor can be expressed by $1/Q=1/Q_{\text{intrinsic}}+1/Q_{\text{extrinsic}}$, where $Q_{\text{extrinsic}}$, limited by the extrinsic losses, would increase with the surface-to-volume ratio of the cavity. It is likely that the low values of $Q_{\text{extrinsic}}$, which diminishes with the increasing duty cycle r/a , masks the high intrinsic Q factor expected of the merged constellation. The experimental Q factor can be further improved by increasing the period of region B or designing region B for each cavity configuration to ensure the lasing mode locates in the middle of its bandgap, so that lateral confinement is enhanced. Surface passivation that can smooth the etched hole sidewalls could also alleviate scattering losses.

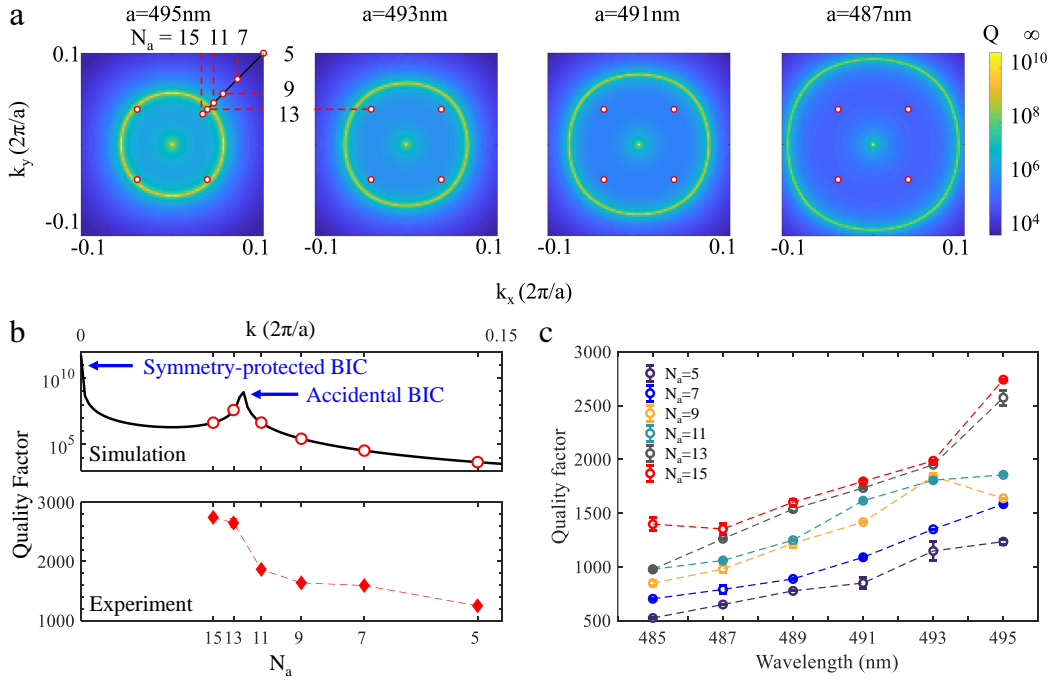


Figure 4. Enhancement of the Q factor by topological engineering. a. The high-Q ring arising from the constellation of multiple BICs appears on bulk band TE A in momentum space. When the period a varies from 485 nm to 495 nm, the ring shrinks towards the center Γ point and eventually reaches the states of M_{11} for $N_a = 13$ (red circles), increasing the Q factor of M_{11} for $N_a = 13$. **b.** Simulated (red circles in the upper panel) and experimental (red diamonds connected by red dashed line in the lower panel) Q-factor of the lasing M_{11} mode at $a = 495$ nm as the function of cavity size N_a (lower axis) and therefore the function of wave vector k along Γ -M direction. Simulated Q factor of an infinite PhC is also plotted as black solid line, along which the symmetry-protected BIC at Γ point

and the accidental BIC at $k = 0.057$ can be seen. **c.** The measured Q factor of M_{11} for varied N_a , which shows similar increasing trend as period a increases.

Conclusion

Finally, we systematically compare the metrics of reported BIC lasers with different gain materials as well as those of our devices, as presented in **Table 1**.

In general, the generation of CW-pumped BIC lasers are boosted by combining BIC cavities with different lateral mirrors, such as Fano mirror³⁶ or PhC heterostructures³⁷, which significantly enhance the lateral confinement of light. Super-BIC cavity³⁵ can effectively improve the Q factor and therefore achieving relatively low-threshold lasing. However, lateral scattering loss and low pumping efficiency have so far only limited lasing to the pulsed mode. From the perspective of gain materials, quantum confinement materials, such as InGaAsP QWs^{25, 28, 35, 36}, monolayer WS_2 ³⁷ and Perovskite QDs³⁰, have achieved superior performance in lower threshold power due to their carrier confinement in several dimensions. Our devices, by implementing mini-BIC cavities in an InAs/GaAs QD gain material to achieve three-dimensional confinement of both light and carriers, have simultaneously achieved CW pumping with the lowest reported threshold power density and the smallest footprint.

To conclude, we successfully achieve CW pumped O-band mini-BIC lasers fabricated in an InAs/GaAs QD gain material. The smallest of the mini-BIC lasers has only 5×5 unit-cells with a small mode volume of $1.16(\lambda/n)^3$ and exhibits an ultra-low single mode lasing threshold of $17 \mu\text{W}$ (0.074 kW/cm^2), while the lowest threshold of $12 \mu\text{W}$ (0.052 kW/cm^2) is achieved in 7×7 unit cell devices. The lowest threshold power density is significantly reduced by as much as 99.6%, or down by more than two and half orders of magnitude, compared to the only reported monolithic CW BIC laser in III-V semiconductor QW gain material³⁶. By careful engineering of structural parameters, the mini-BIC lasers have also been tuned across a wavelength range of 80 nm.

The mini-BIC lasers, fabricated by membrane transfer technique, can be flexibly implemented on different substrate such as silicon or LiNbO_3 . Moreover, used as a surface-emitting laser based on transverse resonance, our mini-BIC lasers can have a noticeable advantage over vertical-cavity surface-emitting laser (VCSEL) at telecom/mid or far-infrared wavelength, which is based on vertical-cavity resonance and thus highly material dependent in terms of cavity construction. Just as photonic crystal surface-emitting lasers (PCSEL)¹⁶ and topological-cavity surface-emitting laser (TCSEL)⁴⁸, the resonant wavelength of the mini-BIC lasers can be precisely tuned by simply varying the lattice constant of planar cavity, without the strict limitation imposed by the thickness of DBR material. On the other hand, the ability to engineer the lateral confinement can also lead to in-plane emission that couples directly into waveguides, thereby providing efficient, high spectral quality, precisely wavelength engineered miniature laser sources for PICs.

Moving forward, in addition to further optimizing cavity Q factor and reducing threshold, our approach can be combined with p-i-n hetero-junction structures to enable electrical pumped BIC-lasers, as its small size provides opportunities of reducing both

optical and electrical losses during carrier injection and recombination. The ability to confine light and carrier in all-three dimensions may also open a pathway to strong light-matter interaction in BIC cavities leading to the realization of novel quantum light sources.

Table 1. Comparison of the mini-BIC laser with other BIC lasers.

	BIC type	Pump Method	Gain medium	Wavelength (nm)	Cavity size(μm^2)	Threshold peak power (mW)	Threshold power density (kW/cm^2)	Q factor	Ref.
BIC	Symmetry-protected & accidental BIC	Pulse pump	InGaAsP QWs	~1600	—	73	—	—	[25]
			InGaAsP QWs	1551	19×19	15.6	~4	~4701	[28]
	Symmetry-protected BIC	Pulse pump	GaAs	830–850	—	8.8×10^5	7.0×10^4	2750	[26]
			CdSe	632-663	—	5.09×10^8	1.8×10^5	2590	[31]
			Perovskite	552	—	5.28×10^5	4.2×10^4	—	[27]
			IR-792 molecules	~860	—	$\sim 2.16 \times 10^6$	$\sim 2.75 \times 10^4$	~2883	[29]
			Perovskite	549	—	—	4.9×10^5	1119	[32]
Perovskite QDs	~630	—	—	—	11	—	[30]		
BIC in PhC heterostructure	Symmetry-protected BIC	CW pump	monolayer WS ₂	637	137	—	0.144	2500	[37]
Super-BIC	Symmetry-protected & accidental BIC	Pulse pump	InGaAsP QWs	~1600	23×23	0.34	1.47	~7300	[35]
Fano-BIC	Fabry-Perot BIC	CW pump	InGaAsP QWs	1560	~2.2	3.5	12.38	~78000	[36]
Mini-BIC	Symmetry-protected & accidental BIC	CW pump	InAs/GaAs QDs	1303/1328 (MM)	3.4×3.4	1.2×10^{-2}	0.052	790	This work
				1311 (SM)	2.5×2.5	1.7×10^{-2}	0.074	525	

MM: multi-modes; SM: single mode.

Method

Numerical Simulation. The photonic band diagrams and mode characteristics are calculated using a three-dimensional finite-element method (FEM) solver of the COMSOL Multiphysics in the frequency domain. Three-dimensional models are built between two perfect-matching layers (PML), with Floquet periodic boundaries imposed on the four surfaces perpendicular to the slabs. The frequencies and quality (Q) factors of resonances can be obtained by the eigenvalue solver. The modal volume of a cavity is calculated referring to the formula: $V = \int \epsilon(\mathbf{r}) |\mathbf{E}(\mathbf{r})|^2 d^3\mathbf{r} / \max[\epsilon(\mathbf{r}) |\mathbf{E}(\mathbf{r})|^2]$, where $\epsilon(\mathbf{r})$ is the material dielectric constant and $|\mathbf{E}(\mathbf{r})|$ is the electric field strength³⁸.

Growth. The QD samples are grown on semi-insulating GaAs (001) substrates by a solid source molecular beam epitaxy (Veeco GENxplor system). A sketch of the heterostructure is shown in Supplementary Fig. S1(a). It consists of a 200 nm Al_{0.8}Ga_{0.2}As sacrificial layer and a 556 nm GaAs layer. Three layers of high-density ($\sim 5.5 \times 10^{10} \text{ cm}^{-2}$) InAs QDs separated by 40 nm GaAs barriers are embedded in the middle of the GaAs layer. Each QD layer comprises 2.4 ML InAs covered with a 3.5 nm In_{0.15}Ga_{0.85}As strain-reducing layer. Room-temperature photoluminescence (PL) emission peaking at 1300 nm was observed (Supplementary Fig. S1(b)) with a narrow full-width at half-maximum (FWHM) of 30 meV.

Device fabrication. We first fabricate the photonic crystal slab using electron beam lithography and dry etching processes. Then the top surface of the III-V wafer is bonded to a transparent quartz substrate with $\sim 2.5 \mu\text{m}$ NOA61 via an ultraviolet curing process. Citric- and HF-acids are used to selectively remove the GaAs substrate and the Al_{0.8}Ga_{0.2}As sacrificial layer. After the wet etching, the QD-containing PhC layer is then capped by $\sim 2.5 \mu\text{m}$ NOA61 and a glass plate. The finished sample therefore has

the PhC membrane placed in the middle of $\sim 5 \mu\text{m}$ NOA ($n_{\text{NOA}} = 1.54$) and sandwiched between two glass plates ($n=1.49$) to ensure mirror-flip symmetry. Full fabrication details are presented in the Supplementary Information.

Optical characterization. The sample is characterized by means of confocal micro-photoluminescence spectroscopy at room temperature. A 705-nm continuous-wave laser was used to optically excite the device via a 50x objective with a numerical aperture of 0.65. The spot size of the pump laser is $\sim 5.4 \mu\text{m}$ (Supplementary Information Fig. S3). The emitted photons are collected by the same objective and sent to an InGaAs monochromator for spectrum characterization. The resolution of the spectrometer is $\sim 0.20 \text{ nm}$.

Acknowledgement

This work is supported by the the National Natural Science Foundation of China (11704424, 62135012), the National Key R&D Program of China (2018YFB2200201), the Science and Technology Program of Guangzhou (202103030001), the National Key R&D Program of Guangdong Province (2020B0303020001), and the Local Innovative and Research Teams Project of Guangdong Pearl River Talents Program (2017BT01121).

Reference

1. Smit M, Williams K, Tol Jvd. Past, present, and future of InP-based photonic integration. *APL Photonics* 2019, **4**(5): 050901.
2. Ma R-M, Oulton RF. Applications of nanolasers. *Nature Nanotechnology* 2019, **14**(1): 12-22.
3. Margalit N, Xiang C, Bowers SM, Bjorlin A, Blum R, Bowers JE. Perspective on the future of silicon photonics and electronics. *Applied Physics Letters* 2021, **118**(22): 220501.
4. Ning C-Z. Semiconductor nanolasers and the size-energy-efficiency challenge: a review. *Advanced Photonics* 2019, **1**(1): 014002.
5. Miller DAB. Device Requirements for Optical Interconnects to Silicon Chips. *Proceedings of the IEEE* 2009, **97**(7): 1166-1185.
6. Doylend JK, Gupta S. An overview of silicon photonics for LIDAR. *Silicon Photonics XV* 2020, **11285**(11285J).
7. Wang J, Sciarrino F, Laing A, Thompson MG. Integrated photonic quantum technologies. *Nature Photonics* 2020, **14**(5): 273-284.
8. Moody G, Sorger VJ, Blumenthal DJ, Juodawlkis PW, Loh W, Sorace-Agaskar C, *et al.* 2022 Roadmap on integrated quantum photonics. *Journal of Physics: Photonics* 2022, **4**(1): 012501.
9. Jeong K-Y, Hwang M-S, Kim J, Park J-S, Lee JM, Park H-G. Recent Progress in Nanolaser Technology. 2020, **32**(51): 2001996.
10. Hill MT, Gather MC. Advances in small lasers. *Nature Photonics* 2014, **8**(12): 908-918.
11. Akahane Y, Asano T, Song B-S, Noda S. High-Q photonic nanocavity in a two-dimensional photonic crystal. *Nature* 2003, **425**(6961): 944-947.
12. Painter O, Lee RK, Scherer A, Yariv A, O'Brien JD, Dapkus PD, *et al.* Two-Dimensional Photonic Band-Gap Defect Mode Laser. *Science* 1999, **284**(5421): 1819-1821.
13. Song B-S, Noda S, Asano T, Akahane Y. Ultra-high-Q photonic double-heterostructure nanocavity. *Nature Materials* 2005, **4**(3): 207-210.
14. Ellis B, Mayer MA, Shambat G, Sarmiento T, Harris J, Haller EE, *et al.* Ultralow-threshold

- electrically pumped quantum-dot photonic-crystal nanocavity laser. *Nature Photonics* 2011, **5**(5): 297-300.
15. Henry C, Kazarinov R, Logan R, Yen R. Observation of destructive interference in the radiation loss of second-order distributed feedback lasers. *IEEE Journal of Quantum Electronics* 1985, **21**(2): 151-154.
 16. Hirose K, Liang Y, Kurosaka Y, Watanabe A, Sugiyama T, Noda S. Watt-class high-power, high-beam-quality photonic-crystal lasers. *Nature Photonics* 2014, **8**(5): 406-411.
 17. Hsu CW, Zhen B, Lee J, Chua S-L, Johnson SG, Joannopoulos JD, *et al.* Observation of trapped light within the radiation continuum. *Nature* 2013, **499**(7457): 188-191.
 18. Jin J, Yin X, Ni L, Soljačić M, Zhen B, Peng C. Topologically enabled ultrahigh-Q guided resonances robust to out-of-plane scattering. *Nature* 2019, **574**(7779): 501-504.
 19. Lee J, Zhen B, Chua S-L, Qiu W, Joannopoulos JD, Soljačić M, *et al.* Observation and Differentiation of Unique High-Q Optical Resonances Near Zero Wave Vector in Macroscopic Photonic Crystal Slabs. *Physical Review Letters* 2012, **109**(6): 067401.
 20. Liu Z, Xu Y, Lin Y, Xiang J, Feng T, Cao Q, *et al.* High-Q Quasibound States in the Continuum for Nonlinear Metasurfaces. *Physical Review Letters* 2019, **123**(25): 253901.
 21. Hsu CW, Zhen B, Stone AD, Joannopoulos JD, Soljačić M. Bound states in the continuum. *Nature Reviews Materials* 2016, **1**(9): 16048.
 22. Altug H, Englund D, Vučković J. Ultrafast photonic crystal nanocavity laser. *Nature Physics* 2006, **2**(7): 484-488.
 23. Zhou T, Tang M, Xiang G, Xiang B, Hark S, Martin M, *et al.* Continuous-wave quantum dot photonic crystal lasers grown on on-axis Si (001). *Nature Communications* 2020, **11**(1): 977.
 24. Minkov M, Dharanipathy UP, Houdré R, Savona V. Statistics of the disorder-induced losses of high-Q photonic crystal cavities. *Opt Express* 2013, **21**(23): 28233-28245.
 25. Bahari B, Vallini F, Lepetit T, Tellez-Limon R, Park JH, Kodigala A, *et al.* Integrated and Steerable Vortex Lasers using Bound States in Continuum. 2017. arXiv:1707.00181.
 26. Ha ST, Fu YH, Emani NK, Pan Z, Bakker RM, Paniagua-Domínguez R, *et al.* Directional lasing in resonant semiconductor nanoantenna arrays. *Nature Nanotechnology* 2018, **13**(11): 1042-1047.
 27. Huang C, Zhang C, Xiao S, Wang Y, Fan Y, Liu Y, *et al.* Ultrafast control of vortex microlasers. 2020, **367**(6481): 1018-1021.
 28. Kodigala A, Lepetit T, Gu Q, Bahari B, Fainman Y, Kanté B. Lasing action from photonic bound states in continuum. *Nature* 2017, **541**(7636): 196-199.
 29. Mohamed S, Wang J, Rekola H, Heikkinen J, Asamoah B, Shi L, *et al.* Topological charge engineering in lasing bound states in continuum. 2020. arXiv:2012.15642.
 30. Wu M, Ding L, Sabatini RP, Sagar LK, Bappi G, Paniagua-Domínguez R, *et al.* Bound State in the Continuum in Nanoantenna-Coupled Slab Waveguide Enables Low-Threshold Quantum-Dot Lasing. *Nano Letters* 2021, **21**(22): 9754-9760.
 31. Wu M, Ha ST, Shendre S, Durmusoglu EG, Koh W-K, Abujetas DR, *et al.* Room-Temperature Lasing in Colloidal Nanoplatelets via Mie-Resonant Bound States in the Continuum. *Nano Letters* 2020, **20**(8): 6005-6011.
 32. Wang Y, Fan Y, Zhang X, Tang H, Song Q, Han J, *et al.* Highly Controllable Etchless Perovskite Microlasers Based on Bound States in the Continuum. *ACS Nano* 2021, **15**(4): 7386-7391.
 33. Takeda K, Sato T, Shinya A, Nozaki K, Kobayashi W, Taniyama H, *et al.* Few-fJ/bit data

- transmissions using directly modulated lambda-scale embedded active region photonic-crystal lasers. *Nature Photonics* 2013, **7**(7): 569-575.
34. Matsuo S, Shinya A, Kakitsuka T, Nozaki K, Segawa T, Sato T, *et al.* High-speed ultracompact buried heterostructure photonic-crystal laser with 13 fJ of energy consumed per bit transmitted. *Nature Photonics* 2010, **4**(9): 648-654.
 35. Hwang M-S, Lee H-C, Kim K-H, Jeong K-Y, Kwon S-H, Koshelev K, *et al.* Ultralow-threshold laser using super-bound states in the continuum. *Nature Communications* 2021, **12**(1): 4135.
 36. Yu Y, Sakanas A, Zali AR, Semenova E, Yvind K, Mørk J. Ultra-coherent Fano laser based on a bound state in the continuum. *Nature Photonics* 2021, **15**(10): 758-764.
 37. Ge X, Minkov M, Fan S, Li X, Zhou W. Laterally confined photonic crystal surface emitting laser incorporating monolayer tungsten disulfide. *npj 2D Materials and Applications* 2019, **3**(1): 16.
 38. Chen Z, Yin X, Jin J, Zheng Z, Zhang Z, Wang F, *et al.* Observation of miniaturized bound states in the continuum with ultra-high quality factors. *Science Bulletin* 2022, **67**(4): 359-366.
 39. Liu HY, Liew SL, Badcock T, Mowbray DJ, Skolnick MS, Ray SK, *et al.* p-doped 1.3 μ m InAs/GaAs quantum-dot laser with a low threshold current density and high differential efficiency. *Applied Physics Letters* 2006, **89**(7): 073113.
 40. Kageyama T, Nishi K, Yamaguchi M, Mochida R, Maeda Y, Takemasa K, *et al.* Extremely high temperature (220°C) continuous-wave operation of 1300-nm-range quantum-dot lasers. *2011 Conference on Lasers and Electro-Optics Europe and 12th European Quantum Electronics Conference (CLEO EUROPE/EQEC)* 2011, 22-26 May 2011. 1-1.
 41. Shchekin OB, Deppe DG. 1.3 μ m InAs quantum dot laser with $T_0=161$ K from 0 to 80°C. *Applied Physics Letters* 2002, **80**(18): 3277-3279.
 42. Chen S, Li W, Wu J, Jiang Q, Tang M, Shutts S, *et al.* Electrically pumped continuous-wave III-V quantum dot lasers on silicon. *Nature Photonics* 2016, **10**(5): 307-311.
 43. Hantschmann C, Liu Z, Tang M, Chen S, Seeds AJ, Liu H, *et al.* Theoretical Study on the Effects of Dislocations in Monolithic III-V Lasers on Silicon. *Journal of Lightwave Technology* 2020, **38**(17): 4801-4807.
 44. Norman JC, Jung D, Zhang Z, Wan Y, Liu S, Shang C, *et al.* A Review of High-Performance Quantum Dot Lasers on Silicon. *IEEE Journal of Quantum Electronics* 2019, **55**(2): 1-11.
 45. Iwahashi S, Kurosaka Y, Sakai K, Kitamura K, Takayama N, Noda S. Higher-order vector beams produced by photonic-crystal lasers. *Opt Express* 2011, **19**(13): 11963-11968.
 46. Streifer W, Scifres D, Burnham R. Coupling coefficients for distributed feedback single- and double-heterostructure diode lasers. *IEEE Journal of Quantum Electronics* 1975, **11**(11): 867-873.
 47. Yang Y, Peng C, Liang Y, Li Z, Noda S. Analytical Perspective for Bound States in the Continuum in Photonic Crystal Slabs. *Physical Review Letters* 2014, **113**(3): 037401.
 48. Yang L, Li G, Gao X, Lu L. Topological-cavity surface-emitting laser. *Nature Photonics* 2022, **16**(4): 279-283.